

## KMT-2025-BLG-1616Lb: First Microlensing Bound Planet From DREAMS

HONGJING YANG (杨弘靖),<sup>1,2</sup> WEICHENG ZANG (臧伟呈),<sup>3,2</sup> YOON-HYUN RYU,<sup>4</sup> TAKAHIRO SUMI,<sup>5</sup> JIYUAN ZHANG (张纪元),<sup>6</sup> HONGYU LI (李弘禹),<sup>6</sup> AND CHEONGHO HAN<sup>7</sup>  
 (LEADING AUTHORS)

YUCHEN TANG,<sup>2</sup> QIYUE QIAN,<sup>6</sup> ZHIXING LI,<sup>6</sup> YUXIN SHANG,<sup>6</sup> XIKAI SHAN,<sup>6</sup> SHUDE MAO,<sup>2</sup> GUILLERMO DAMKE,<sup>8</sup>  
 ALFREDO ZENTENO,<sup>8</sup> STEVE HEATHCOTE,<sup>8</sup> KONSTANTINA BOUTSIA,<sup>8</sup> PRZEMEK MRÓZ,<sup>9</sup> XIURUI ZHAO,<sup>10</sup> MATTHEW PENNY,<sup>11</sup>  
 SEAN TERRY,<sup>12,13</sup> PATRICK TAMBURRO,<sup>3</sup> TIMOTHY CUNNINGHAM,<sup>3</sup> QUANZHI YE,<sup>13,14</sup> ERIC W. PENG,<sup>15</sup> RACHEL STREET,<sup>16</sup>  
 KATARZYNA KRUSZYŃSKA,<sup>16</sup> ETIENNE BACHELET,<sup>17</sup> YIANNIS TSAPRAS,<sup>18</sup> AND MARKUS HUNDERTMARK<sup>18</sup>  
 (THE DREAMS COLLABORATION)

MICHAEL D. ALBROW,<sup>19</sup> SUN-JU CHUNG,<sup>20</sup> ANDREW GOULD,<sup>21,22</sup> KYU-HA HWANG,<sup>20</sup> YOUN KIL JUNG,<sup>20,23</sup> IN-GU SHIN,<sup>2</sup>  
 YOSSI SHVARTZVALD,<sup>24</sup> JENNIFER C. YEE,<sup>3</sup> DONG-JIN KIM,<sup>20</sup> CHUNG-UK LEE,<sup>20</sup> AND BYEONG-GON PARK<sup>20</sup>  
 (THE KMTNET COLLABORATION)

DAVID P. BENNETT,<sup>12,13</sup> IAN A. BOND,<sup>25</sup> GIUSEPPE CATALDO,<sup>26</sup> RYUSEI HAMADA,<sup>5</sup> YUKI HIRAO,<sup>27</sup> ASAHI IDEI,<sup>5</sup> SHUMA MAKIDA,<sup>5</sup>  
 SHOTA MIYAZAKI,<sup>28</sup> TUTUMI NAGAI,<sup>5</sup> TOGO NAGANO,<sup>5</sup> SEIYA NAKAYAMA,<sup>5</sup> MAYU NISHIO,<sup>5</sup> KANSUKE NUNOTA,<sup>5</sup> RYO OGAWA,<sup>5</sup>  
 RYUNOSUKE OISHI,<sup>5</sup> YUI OKUMOTO,<sup>5</sup> NICHOLAS J. RATTENBURY,<sup>29</sup> YUKI K. SATOH,<sup>30</sup> DAISUKE SUZUKI,<sup>5</sup>  
 MOTOHIDE TAMURA,<sup>31,32</sup> TAKUTO TAMAOKI,<sup>5</sup> AND HIBIKI YAMA<sup>5</sup>  
 (THE PRIME COLLABORATION)

<sup>1</sup>Westlake Institute for Advanced Study, Hangzhou 310030, Zhejiang Province, China

<sup>2</sup>Department of Astronomy, Westlake University, Hangzhou 310030, Zhejiang Province, China

<sup>3</sup>Center for Astrophysics | Harvard & Smithsonian, 60 Garden St., Cambridge, MA 02138, USA

<sup>4</sup>Korea Astronomy and Space Science Institute, Daejeon 34055, Republic of Korea

<sup>5</sup>Department of Earth and Space Science, Graduate School of Science, The University of Osaka, Toyonaka, Osaka 560-0043, Japan

<sup>6</sup>Department of Astronomy, Tsinghua University, Beijing 100084, China

<sup>7</sup>Department of Physics, Chungbuk National University, Cheongju 28644, Republic of Korea

<sup>8</sup>Cerro Tololo Inter-American Observatory/NSF's NOIRLab, Casilla 603, La Serena, Chile

<sup>9</sup>Astronomical Observatory, University of Warsaw, Al. Ujazdowskie 4, 00-478 Warszawa, Poland

<sup>10</sup>Cahill Center for Astrophysics, California Institute of Technology, 1216 East California Boulevard, Pasadena, 91125, CA, USA

<sup>11</sup>Department of Physics and Astronomy, Louisiana State University, Baton Rouge, LA 70803, USA

<sup>12</sup>Code 667, NASA Goddard Space Flight Center, Greenbelt, MD 20771, USA

<sup>13</sup>Department of Astronomy, University of Maryland, College Park, MD 20742, USA

<sup>14</sup>Center for Space Physics, Boston University, 725 Commonwealth Ave, Boston, MA 02215, USA

<sup>15</sup>NSF NOIRLab, 950 N. Cherry Avenue, Tucson, AZ 85719, USA

<sup>16</sup>Las Cumbres Observatory Global Telescope Network, Inc., 6740 Cortona Drive, Suite 102, Goleta, CA 93117, USA

<sup>17</sup>IPAC, Mail Code 100-22, Caltech, 1200 E. California Blvd., Pasadena, CA 91125, USA

<sup>18</sup>Astronomisches Rechen-Institut, Mönchhofstr. 12-14, D-69120 Heidelberg, Germany

<sup>19</sup>University of Canterbury, School of Physical and Chemical Sciences, Private Bag 4800, Christchurch 8020, New Zealand

<sup>20</sup>Korea Astronomy and Space Science Institute, Daejeon 34055, Republic of Korea

<sup>21</sup>Max-Planck-Institute for Astronomy, Königstuhl 17, 69117 Heidelberg, Germany

<sup>22</sup>Department of Astronomy, Ohio State University, 140 W. 18th Ave., Columbus, OH 43210, USA

<sup>23</sup>National University of Science and Technology (UST), Daejeon 34113, Republic of Korea

<sup>24</sup>Department of Particle Physics and Astrophysics, Weizmann Institute of Science, Rehovot 7610001, Israel

<sup>25</sup>School of Mathematical and Computational Sciences, Massey University, Auckland 0745, New Zealand

<sup>26</sup>NASA Goddard Space Flight Center, Greenbelt, MD 20771, USA

<sup>27</sup>Institute of Astronomy, Graduate School of Science, The University of Tokyo, 2-21-1 Osawa, Mitaka, Tokyo 181-0015, Japan

<sup>28</sup>Institute of Space and Astronautical Science, Japan Aerospace Exploration Agency, 3-1-1 Yoshinodai, Chuo, Sagamihara, Kanagawa 252-5210, Japan

<sup>29</sup>Department of Physics, University of Auckland, Private Bag 92019, Auckland, New Zealand

<sup>30</sup>College of Science and Engineering, Kanto Gakuin University, Yokohama, Kanagawa 236-8501, Japan

<sup>31</sup>Astrobiology Center, 2-21-1 Osawa, Mitaka-shi, Tokyo 181-8588, Japan

<sup>32</sup>Department of Astronomy, University of Tokyo, 7-3-1 Hongo, Bunkyo-ku, Tokyo 113-0033, Japan

## ABSTRACT

We present observations and analysis of the bound planetary microlensing event KMT-2025-BLG-1616. The planetary signal was captured by the Korea Microlensing Telescope Network (KMTNet) and the DECam Rogue Earths and Mars Survey (DREAMS). DREAMS's minute-cadence observations break the central/resonant degeneracy in the binary-lens models. The color of the faint source star ( $I = 22$ ) is measured from the DREAMS's  $r - z$  color. The planetary system has a planet-host mass ratio of  $q \sim 5 \times 10^{-4}$ . A Bayesian analysis yields a host-star mass of  $\sim 0.3 M_{\odot}$ , a planetary mass of  $\sim 40 M_{\oplus}$ , a projected planet-host separation of  $\sim 1.6$  au, and a lens distance of  $\sim 7.5$  kpc. Based on the photometric precision achieved by DREAMS for this event, we simulate free-floating planet (FFPs) detections and find that DREAMS is sensitive to Mars-mass FFPs in the Galactic bulge and Moon-mass FFPs in the Galactic disk.

## 1. INTRODUCTION

The gravitational microlensing technique is sensitive to wide-orbit planets (Mao & Paczynski 1991; Gould & Loeb 1992) and to free-floating planets (FFPs) (Sumi et al. 2011). Two main challenges for microlensing planet searches are the low event rate and the short duration of planetary signals. To overcome the challenges, the first phase searches adopted the two-step strategy proposed by Gould & Loeb (1992): large-area ( $\sim 100 \text{ deg}^2$ ), low-cadence surveys  $\Gamma \lesssim 1 \text{ day}^{-1}$  to identify microlensing events, with high-cadence follow-up to capture planetary perturbations (e.g., Udalski et al. 2005; Dong et al. 2009; Beaulieu et al. 2006). This approach produced two homogeneous samples of bound planets and indicated that Neptune-class planets on wide orbits are common (Gould et al. 2010; Cassan et al. 2012), but it is poorly suited to detecting FFPs.

With the deployment of wide-field cameras on 1–2 meter telescopes, the second phase of microlensing planetary search, including the second phase of Microlensing Observations in Astrophysics (MOA-II, 2006+, Sako et al. 2008), the fourth phase of the Optical Gravitational Lensing Experiment (OGLE-IV, 2011+, Udalski et al. 2015), the Wise microlensing survey (2011–2014, Shvartzvald et al. 2016), the Korea Microlensing Telescope Network (KMTNet, 2016+, Kim et al. 2016), the Prime Focus Infrared Microlensing Experiment (PRIME, 2024+, Sumi et al. 2025), has carried out large-area monitoring with cadences ranging from  $\Gamma \sim 1 \text{ day}^{-1}$  to  $\sim 6 \text{ hr}^{-1}$ . These survey-only programs have discovered more than 200 bound planets (Christiansen et al. 2025) and produced four statistical samples (Shvartzvald et al. 2016; Suzuki et al. 2016; Poleski et al. 2021; Zang et al. 2025). The largest of these samples (Zang et al. 2025) suggests two populations of wide-orbit planets: gas giants and super-Earths/mini-Neptunes. At the same time, pure survey searches have reported  $> 10$  candidate FFPs (e.g., Mróz et al. 2017, 2020; Gould et al. 2022; Koshimoto et al. 2023). If confirmed, these detections would imply that terrestrial- and super-Earth-mass FFPs are several to dozens of times

more numerous than bound planets or other stellar objects (Mróz et al. 2017; Gould et al. 2022; Sumi et al. 2023).

The FFP mass functions inferred by Gould et al. (2022) and Sumi et al. (2023) favor a power-law index near  $-1$ . If this trend extends to Mars- and even Moon-mass scales, the implied occurrence rate would exceed that inferred from current second-generation microlensing surveys by one to two orders of magnitude. In this low-mass regime, finite-source effects dominate the light curves' morphology, and as a result, the event rate scales with the occurrence rate of FFPs and independent of the angular Einstein radius and thus the mass (Gould et al. 2021). Consequently, wide-area coverage ( $\sim 100 \text{ deg}^2$ ) is unnecessary and a small-area survey (a few square degrees) with sufficient photometric precision and high cadence can efficiently detect low-mass FFPs.

Based on this idea, the DECam Rogue Earths And Mars Survey (DREAMS)<sup>1</sup>, using the  $3 \text{ deg}^2$  Dark Energy Camera (DECam; Honscheid & DePoy 2008; Flaugher et al. 2015) on the 4 m Blanco telescope at Cerro Tololo Inter-American Observatory (CTIO) in Chile, has been surveying a  $5 \text{ deg}^2$  field since June 2025. With the larger aperture and a cadence of one exposure every 1–2 minutes, DREAMS accumulates about 50–500 times more source-star flux over the same sky area than other microlensing surveys, yielding substantially higher sensitivity to low-mass FFPs.

Beyond its high sensitivity to low-mass FFPs, DREAMS can also recover weak planetary signals in bound systems that other microlensing surveys miss or cannot adequately characterize. Such signals can arise from very low planet-host mass ratios ( $q$ ; to date, only one planet with  $\log q < -5$  has been discovered; Zang et al. 2025), from weak cusp crossings, or from high-magnification events that require higher cadence and photometric precision (e.g., KMT-2022-BLG-0440; Zang et al. 2023).

Here we present the first bound planet reported by DREAMS, KMT-2025-BLG-1616Lb, identified during a high-magnification event. The structure of this paper is as

<sup>1</sup> <https://time-allocation.noirlab.edu/#/proposal/details/560332>

follows. In Section 2 we describe the KMTNet, PRIME, and DREAMS observations of this event. Section 3 presents the light-curve analysis, and Section 4 details the source and lens properties. Finally, in Section 5 we present results using KMTNet and PRIME data only and estimate DREAMS’s detection limits for FFPs.

## 2. OBSERVATIONS

Figure 1 displays all light curves acquired for KMT-2025-BLG-1616. The source of this event lies at equatorial coordinates of  $(\alpha, \delta)_{\text{J2000}} = (17:51:06.93, -30:08:20.80)$ , corresponding to Galactic coordinates of  $(\ell, b) = (-0.4137, -1.6445)$  deg. The event was first detected by the KMTNet AlertFinder (Kim et al. 2018b) at 02:10 UT on 2025 July 2 (HJD’ = 10858.59, HJD’ = HJD – 2450000). Because KMTNet issued the alert about 20 hours after the event peak, no follow-up observations were obtained from the KMTNet high-magnification follow-up program (Zang et al. 2021a). The event was independently flagged by the PRIME team 25 hours later as PRIME-2025-BLG-0254.

KMTNet observations were conducted using its three identical 1.6-meter telescopes located at the Siding Spring Observatory (SSO) in Australia (KMTA), CTIO (KMTC), and the South African Astronomical Observatory (SAAO) in South Africa (KMTS). KMT-2025-BLG-1616 falls in the overlap of two KMTNet fields, BLG01 and BLG42, giving a combined observing cadence of  $4 \text{ hr}^{-1}$ ; see Figure 12 of (Kim et al. 2018a) for the field layout. Most KMTNet images used in the light-curve analysis were taken in the  $I$  band, while  $\sim 9\%$  of frames were obtained in the  $V$  band to measure the source color. Each KMTNet  $V$ -band exposure was taken about 2 minutes before or after a KMTNet  $I$ -band exposure of the same field.

The event is also located in the PRIME GB111 field, which is observed at a cadence of  $2.8 \text{ hr}^{-1}$  (see Figure 13 of Sumi et al. 2025 for the field placement). PRIME took observations using its 2.2-meter telescope at SAAO. Most PRIME images were taken in the  $H$  band, with roughly one  $J$ -band image per night for source-color measurements. The  $J$ -band light curve for this event is excluded from the analysis due to insufficient signal-to-noise ratios (SNRs).

In 2025, DREAMS obtained DECam observations on June 29–July 4 and on September 5, 7, and 8. At the position of this event, the June–July run sampled each hour with five  $z$ -band blocks and one  $r$ -band block. Each block comprised four exposures, with individual exposure times of 42 s in  $z$  and 60 s in  $r$ . Thus, during the peak the DREAMS cadence corresponded to 20  $z$ -band and four  $r$ -band observations per hour. During the September run the cadence was four  $z$ -band blocks and one  $r$ -band block per hour. Each  $z$ -band block contained four images and each  $r$ -band block three images, with exposure times of 60 s in  $z$  and 80 s in  $r$ . Further details

of the DREAMS observations will be provided with the first DREAMS data release (Yang, Zang et al., in preparation).

CFHT performed complementary observations with DREAMS on 2025 June 29–30 and July 1 using the  $1 \text{ deg}^2$  imager MegaCam. However, the event falls in the gap between two CCDs, so no CFHT data are available for this event.

DECam images were initially processed with the DECam Community Pipeline (Valdes et al. 2014), which performs calibration using reference frames, removes instrumental signatures, and identifies and rejects cosmic rays. The data used in the light-curve analysis were re-reduced with difference imaging analysis (DIA; Tomaney & Croots 1996; Alard & Lupton 1998) as implemented by each group: Albrown et al. (2009) and Yang et al. (2024, 2025) for KMTNet and DREAMS, and Bond et al. (2001) for PRIME. The photometric uncertainties produced by the DIA pipelines were renormalized following the procedure of Yee et al. (2012), such that the reduced chi-squared ( $\chi^2/\text{dof}$ ) for each dataset is unity. The  $V$ - and  $I$ -band magnitudes reported in this paper are calibrated to the standard system using the OGLE-III stellar catalog (Szymański et al. 2011), while the  $z$ - and  $r$ -band magnitudes are the DECam instrumental magnitude.

## 3. LIGHT-CURVE ANALYSIS

As seen in Figure 1, the observed light curves of KMT-2025-BLG-1616 deviate from the single-lens single-source (1L1S) model (dashed line). A 1L1S model has three Paczyński parameters (Paczyński 1986):  $t_0$ ,  $u_0$ , and  $t_E$ . These denote, respectively, the time of closest approach of the source to the lens-mass center, the impact parameter in units of the angular Einstein radius  $\theta_E$ , and the Einstein-radius crossing time. The timescale  $t_E$  is related to the lens mass  $M_L$ , the lens-source relative parallax  $\pi_{\text{rel}}$ , the relative proper motion  $\mu_{\text{rel}}$ , and  $\theta_E$  via

$$t_E = \frac{\theta_E}{\mu_{\text{rel}}}; \quad \theta_E = \sqrt{\kappa M_L \pi_{\text{rel}}}; \quad (1)$$

$$\kappa \equiv \frac{4G}{c^2 \text{au}} \simeq 8.144 \text{ mas } M_{\odot}^{-1}.$$

The fourth 1L1S parameter is the normalized source size,  $\rho \equiv \theta_{*}/\theta_E$ , where  $\theta_{*}$  is the angular radius of the source (Witt & Mao 1994).

We fit the light curves with the binary-lens single-source (2L1S, Mao & Paczynski 1991; Gould & Loeb 1992) model. A static binary-lens geometry is specified by three parameters:  $(q, s, \alpha)$ , denoting the binary mass ratio, the projected separation (in units of the Einstein radius), and the angle between the source trajectory and the binary axis, respectively.

In addition to the seven parameters that determine the magnification over time  $f(t)$ , for each data set  $i$ , we include two flux parameters,  $(f_{S,i}, f_{B,i})$ , representing the source flux and any blended flux (from unrelated stars or possible lens light).

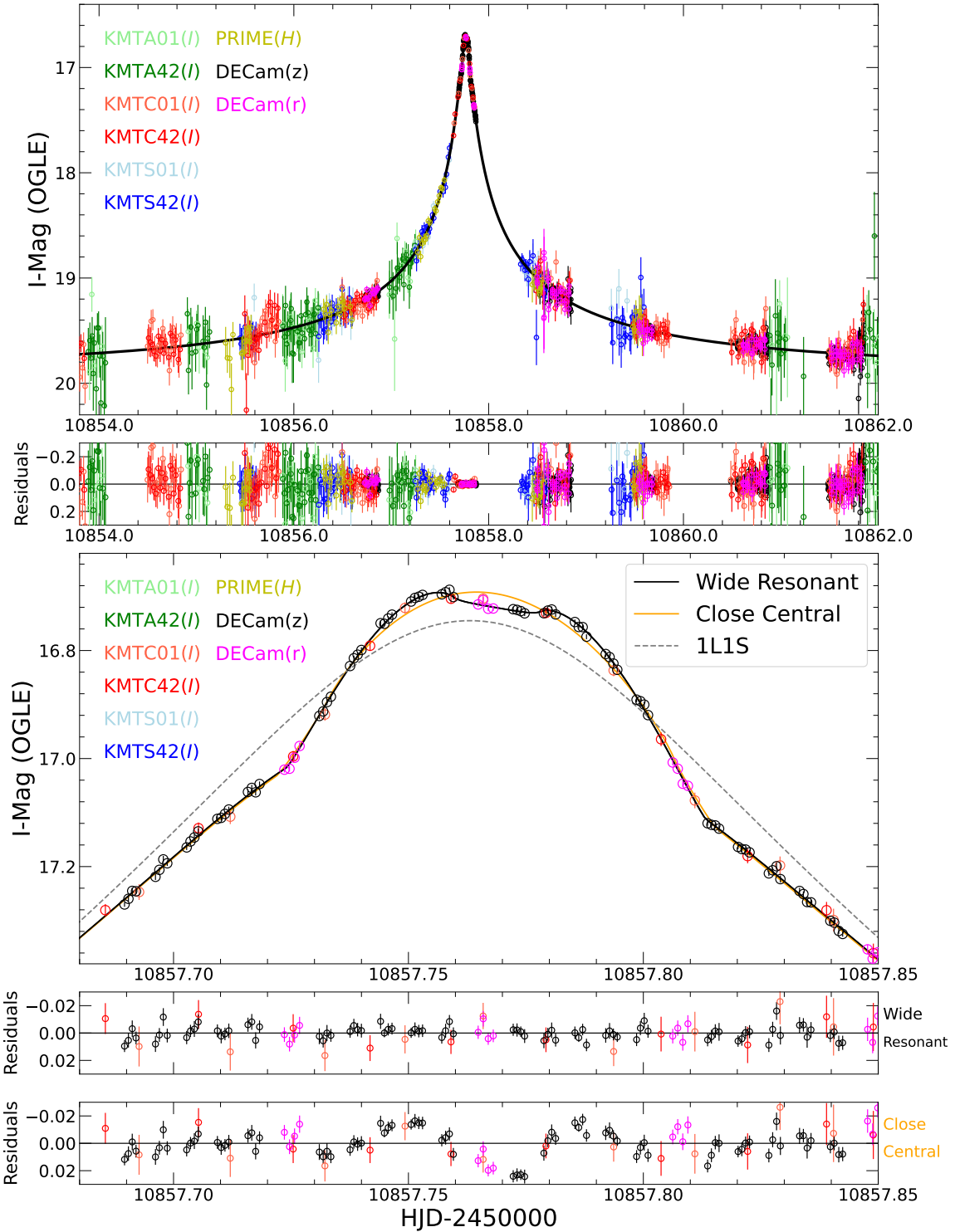


**Figure 1.** Light curve of the microlensing event, KMT-2025-BLG-1616, with the 2L1S models (solid black and orange lines) and the underlying 1L1S model (dashed grey line). Different data sets are plotted in different colors. The upper panels shows the 8-day data around the peak. The lower panels present a close-up of the planetary anomaly and the residuals relative to the 2L1S models.

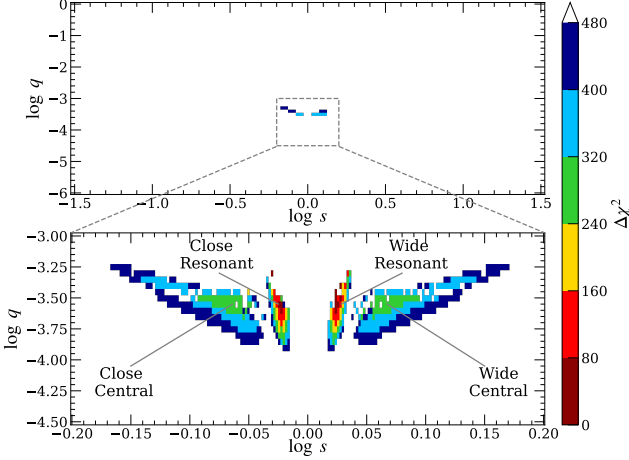


**Figure 2.** The  $\chi^2$  surface in the  $(\log s, \log q)$  plane obtained from the 2L1S grid search. The upper panel shows the coarse grid, while the lower panel zooms in on the dense grid around the global minimum. Dark red, red, yellow, green, blue, and dark blue denote grid points within  $\Delta\chi^2 < 1n, < 2n, < 3n, < 4n, < 5n$ , and  $< 6n$ , respectively, where  $n = 80$ . Grid points with  $\Delta\chi^2 > 480$  are left blank. The labels “Close Central”, “Wide Central”, “Close Resonant”, and “Wide Resonant” in the lower panel mark the four local minima.

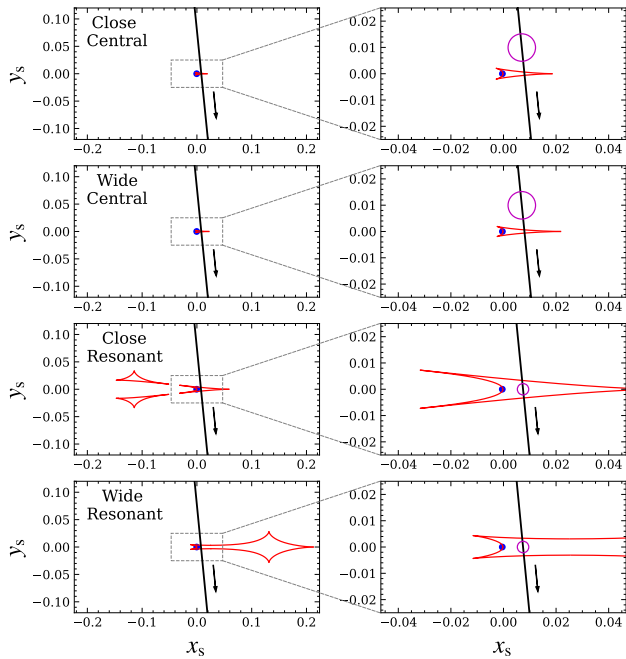


**Figure 3.** Caustic geometries of the four 2L1S solutions. In each panel, the red lines show the caustic, the blue dot marks the location of the host star, the black line represents the source-lens relative trajectory, and the arrow indicates the direction of source motion. The right panels provide close-up views of the caustic-crossing regions, with the radii of the magenta circles indicating the source size.

The observed flux is modeled as

$$f_i(t) = f_{S,i} A(t) + f_{B,i}, \quad (2)$$

where  $A(t)$  is the 2L1S magnification as a function of time and computed with the contour-integration code `VBBinaryLensing` (Bozza 2010; Bozza et al. 2018, 2025).

We incorporate the source surface brightness with a linear limb-darkening law (An et al. 2002; Claret & Bloemen 2011). Using the intrinsic source color derived in Section 4 together with the color-temperature relations of Houdashelt et al. (2000), we estimate an effective temperature of  $\sim 4830$  K. Assuming  $\log g = 2.5$ , solar metallicity, and a microturbulent velocity of  $1 \text{ km s}^{-1}$ , we adopt the following linear limb-darkening coefficients from Claret & Bloemen (2011):  $u_I = 0.57$  ( $I$  band),  $u_z = 0.53$  ( $z$  band),  $u_r = 0.70$  ( $r$  band), and  $u_H = 0.36$  ( $H$  band).

To systematically explore the 2L1S parameter space and identify all local  $\chi^2$  minima, we adopt a two-stage grid-search strategy. We first run a sparse grid over  $(\log s, \log q, \log \rho, \alpha)$  and then refine the solution in the neighborhood of the candidate minima. The coarse grid samples 61 values in  $-1.5 \leq \log s \leq 1.5$ , 61 values in  $-6 \leq \log q \leq 0$ , 9 values in  $-4.0 \leq \log \rho \leq -1.6$ , and 16 trial angles uniformly in  $0 \leq \alpha < 2\pi$ . At each grid point we perform a  $\chi^2$  minimization with the `emcee` ensemble sampler (Foreman-Mackey et al. 2013), holding  $(\log s, \log q, \log \rho)$  fixed while allowing  $(t_0, u_0, t_E, \alpha)$  to vary. As shown in the upper panel of Figure 2, distinct minima are found within  $-0.2 \leq \log s \leq 0.2$ ,  $-4.5 \leq \log q \leq -3.0$ , and  $-3.1 \leq \log \rho \leq -1.9$ . We therefore carry out a dense follow-up grid comprising 201 values in  $-0.2 \leq \log s \leq 0.2$ , 31 values in  $-4.5 \leq \log q \leq -3.0$ , 13 values in  $-3.1 \leq \log \rho \leq -1.9$ , and 16 initial angles that uniformly sample  $0 \leq \alpha < 2\pi$ .

The dense grid search yields four distinct minima, as shown in the lower panel of Figure 2. We then refine each solution with MCMC, allowing all seven 2L1S parameters to vary. Final best-fit models and corresponding  $\chi^2$  are obtained via a downhill minimization<sup>2</sup>. Table 1 lists the corresponding 2L1S parameters with their mean values and  $1\sigma$  uncertainties derived from the MCMC posteriors and the  $\chi^2$  from the downhill minimization. Figure 3 shows the caustic structures and source trajectories for these solutions.

The four solutions form two close-wide degenerate pairs related approximately by the transformation  $s \leftrightarrow s^{-1}$  (Grest & Safizadeh 1998), with the remaining parameters nearly unchanged. In one pair, the source crosses the central caus-

<sup>2</sup> We use the Nelder-Mead simplex implementation in `SCIPY`; see <https://docs.scipy.org/doc/scipy/reference/generated/scipy.optimize.fmin.html#scipy.optimize.fmin>.

**Table 1.** Lensing Parameters using Full Data

Parameters	Central		Resonant	
	Close	Wide	Close	Wide
$\chi^2/\text{dof}$	11762.9/11437	11764.8/11437	11437.5/11437	<b>11433.9/11437</b>
$t_0 - 10857$ (HJD')	$0.76297 \pm 0.00008$	$0.76298 \pm 0.00008$	$0.76311 \pm 0.00008$	<b><math>0.76310 \pm 0.00008</math></b>
$u_0 (10^{-3})$	$7.93 \pm 0.29$	$7.93 \pm 0.30$	$7.40 \pm 0.28$	<b><math>7.41 \pm 0.27</math></b>
$t_E$ (days)	$7.91 \pm 0.27$	$7.91 \pm 0.28$	$8.05 \pm 0.29$	<b><math>8.03 \pm 0.28</math></b>
$\rho (10^{-3})$	$5.22 \pm 0.18$	$5.23 \pm 0.19$	$2.16 \pm 0.09$	<b><math>2.18 \pm 0.09</math></b>
$\alpha$ (rad)	$4.8127 \pm 0.0035$	$4.8125 \pm 0.0034$	$4.8115 \pm 0.0028$	<b><math>4.8095 \pm 0.0028</math></b>
$s$	$0.8637 \pm 0.0050$	$1.1678 \pm 0.0065$	$0.9443 \pm 0.0010$	<b><math>1.0678 \pm 0.0012</math></b>
$q (10^{-4})$	$4.72 \pm 0.24$	$4.75 \pm 0.26$	$4.81 \pm 0.22$	<b><math>4.87 \pm 0.23</math></b>
$\log q$	$-3.325 \pm 0.022$	$-3.323 \pm 0.024$	$-3.318 \pm 0.020$	<b><math>-3.312 \pm 0.020</math></b>
$I_S$	$22.036 \pm 0.039$	$22.037 \pm 0.041$	$22.054 \pm 0.040$	<b><math>22.054 \pm 0.040</math></b>

tic. Because the source is larger than the caustic width, the resulting light curve shows a single smooth bump over the peak (Figure 1). In the other pair, the source is smaller than the caustic width, producing a “U”-shaped profile, two caustic crossings connected by a trough. Following the nomenclature of Yang et al. (2022); Zhang et al. (2023); Bell et al. (2024), we designate these as “Close Central” and “Wide Central” for the first pair, and “Close Resonant” and “Wide Resonant” for the second pair. We note that the “Wide Resonant” solution exhibits the six-sided resonant caustic, whereas the “Close Resonant” solution is not strictly resonant. However, its topology is “near-resonant” as proposed by Yee et al. (2021), for which the central and planetary caustics nearly merge, so we retain the resonant designation for this pair.

The “Wide Resonant” solution provides the best fit to the light curves, with the “Close Resonant” solution only slightly disfavored by  $\Delta\chi^2 = 3.8$ . In contrast, the “Close Central” and “Wide Central” solutions are clearly disfavored by  $\Delta\chi^2 \sim 330$ . As shown by the residuals in Figure 1, the “Central” solutions fail to reproduce the “U”-shaped profile. We therefore exclude the “Close Central” and “Wide Central” solutions and retain the “Close Resonant” and “Wide Resonant” solutions as the viable lensing interpretations of this event. This event provides another example for which the “Central/Resonant” degeneracy is resolved by the light curves (e.g., Zhang et al. 2023). The planet-host mass ratio,  $q \sim 5 \times 10^{-4}$ , indicates the presence of a planet in the lens system.

Due to the very faint source ( $I_S \sim 22.1$  mag) and short timescale ( $t_E = 8.0 \pm 0.3$  days), adding microlensing parallax  $\pi_E$  (Gould 1992, 2000) improves the fit by only  $\Delta\chi^2 < 0.3$ . The parallax components are unconstrained, with  $1\sigma$  uncertainties  $> 1$  in all directions, whereas a typical value is

$\sim 0.1$ . We therefore conclude that this event has no meaningful constraint on parallax.

#### 4. SOURCE AND LENS PROPERTIES

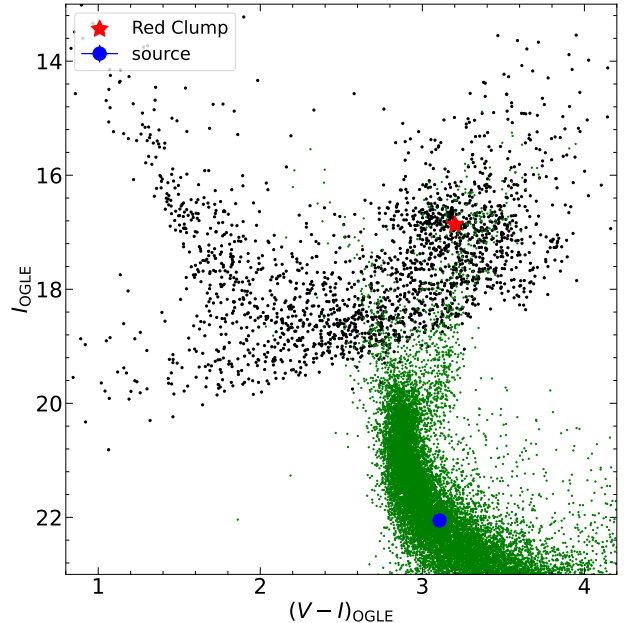


**Figure 4.** Color-magnitude diagram for KMT-2025-BLG-1616. Black dots show OGLE-III field stars (Szymański et al. 2011) within a  $1.5'$  from the event position. The red asterisk and blue dot mark the centroid of the red clump and the source star, respectively. Green points show the HST CMD from Holtzman et al. (1998), and the HST red clump centroid,  $(V - I, I)_{\text{cl}, \text{HST}} = (1.62, 15.15)$  (Bennett et al. 2008), has been shifted to match the OGLE-III red clump.

##### 4.1. Color-Magnitude Diagram

We estimate the intrinsic color and magnitude of the source by placing it on a color-magnitude diagram (CMD) (Yoo et al. 2004). We construct a  $V - I$  versus  $I$  CMD from OGLE-III field stars (Szymański et al. 2011) within  $1.5'$  from the event position. As shown in Figure 4, the red clump (RC) appears to exhibit an elongated distribution. We find that this apparent elongation is mainly caused by very red stars with magnitudes around  $I \sim 17.5$  and colors of  $V - I \gtrsim 3.6$ , for which the OGLE-III  $V$ -band photometric uncertainties are relatively large. Removing these stars and using the method of Nataf et al. (2013), we obtain the centroid of the red clump as  $(V - I, I)_{\text{cl}} = (3.202 \pm 0.009, 16.865 \pm 0.016)$ . The de-reddened color and magnitude of the red clump are  $(V - I, I)_{\text{cl},0} = (1.06 \pm 0.03, 14.47 \pm 0.04)$ , adopted from Bensby et al. (2013) and Nataf et al. (2013), so the extinction and reddening toward the event direction are  $A_I = 2.395 \pm 0.043$  and  $E(V - I) = 2.142 \pm 0.031$ , respectively.

The source color is first derived via a regression of the KMTC01  $V$  versus  $I$  fluxes as a function of magnification and then a calibration to the OGLE-III magnitude system. However, because the event is faint, there is only a single KMTC01  $V$ -band measurement (at  $\text{HJD}' = 10857.666$ ) with a clear magnified signature, yielding  $(V - I)_{\text{S}} = 3.25 \pm 0.23$ , which is too uncertain. There is also one KMTC42  $V$ -band point at higher magnification (at  $\text{HJD}' = 10857.778$ ), but it lies on the anomaly, for which the 2L1S magnifications consider finite-source effects (Gould 1994; Witt & Mao 1994; Nemiroff & Wickramasinghe 1994) and differ between  $I$  and  $V$  due to band-dependent surface brightness. Even ignoring this effect, we obtain  $(V - I)_{\text{S}} = 3.21 \pm 0.15$ , which remains too uncertain.

We therefore measure the source color using the DREAMS  $r - z$  color. Unlike KMTNet's  $V$ -band protocol, for which an  $I$ -band exposure is taken within  $\sim 2$  min of each  $V$ -band exposure, DREAMS acquires  $r$  and  $z$  data in separate blocks, with a typical gap of  $\sim 10$  min between an  $r$  block and the nearest  $z$  block. Accordingly, we first bin each  $r$ -band block to a single point and then bin all  $z$ -band measurements taken within 15 min of that binned  $r$  point. The resulting pairs of binned  $r$  and  $z$  points are used in a linear regression to derive the source color. The mean  $r$ - $z$  time offset is 2.7 min.

We exclude three DREAMS  $r$ -band blocks obtained during finite-source effects at  $\text{HJD}' = 10857.72$ , 10857.76, and 10857.81. Our procedure yields  $(r - z)_{\text{S,DECam}} = 1.212 \pm 0.006$ , consistent with the MCMC posterior mean,  $(r - z)_{\text{S,DECam}} = 1.200$ , from the 2L1S modeling. Calibrating with bright field stars common to the OGLE-III and DECam images yields  $(V - I)_{\text{S}} = 3.106 \pm 0.016$ , which is sufficiently precise. The source's intrinsic color and magnitude are then  $(V - I, I)_{\text{S},0} = (0.96 \pm 0.04, 19.66 \pm 0.06)$ . In Figure 4, we also align the *HST* CMD from Holtzman et al. (1998) with the OGLE-III CMD. This comparison shows that

the source color derived from the DREAMS  $r - z$  color is typical for a star with  $I_0 = 19.66$ .

Applying the color-surface-brightness relation of Adams et al. (2018), we derive an angular source radius of  $\theta_* = 0.470 \pm 0.026 \mu\text{as}$ . This implies

$$\theta_E = \frac{\theta_*}{\rho} = \begin{cases} 0.217 \pm 0.014 \text{ mas} & \text{for Close Resonant, (3)} \\ 0.216 \pm 0.014 \text{ mas} & \text{for Wide Resonant. (4)} \end{cases}$$

and the geocentric lens-source relative proper motion

$$\mu_{\text{rel}} = \frac{\theta_E}{t_E} = \begin{cases} 9.85 \pm 0.74 \text{ mas yr}^{-1} & \text{for Close Resonant, (5)} \\ 9.82 \pm 0.74 \text{ mas yr}^{-1} & \text{for Wide Resonant. (6)} \end{cases}$$

## 4.2. Bayesian Analysis

The lens mass  $M_L$  and distance  $D_L$  are related to the angular Einstein radius and the microlensing parallax by (Gould 1992, 2000)

$$M_L = \frac{\theta_E}{\kappa \pi_E}, \quad D_L = \frac{\text{au}}{\pi_E \theta_E + \text{au}/D_S}, \quad (7)$$

where  $D_S$  is the source distance. Because this event provides no meaningful constraint on  $\pi_E$ , we estimate the physical parameters of the lens system through a Bayesian analysis, adopting priors from a Galactic model.

Our Galactic prior comprises three components: the lens mass function, the spatial number density distributions of lenses and sources, and their kinematics. For the lens mass function, we adopt the Kroupa (2001) initial mass function, imposing upper-mass cutoffs of  $1.3 M_\odot$  for disk lenses and  $1.1 M_\odot$  for bulge lenses (Zhu et al. 2017). The stellar density profiles for both the disk and the bulge follow the prescriptions in Yang et al. (2021). For the bulge velocity distribution, we use the same framework as Zhu et al. (2017), while the disk kinematics follow the “Model” of Yang et al. (2021), implemented with the `galpy` package (Bovy 2015).

We simulate a sample of  $10^8$  events. For each event  $i$ , characterized by  $(t_{\text{E},i}, \mu_{\text{rel},i}, \theta_{\text{E},i})$ , we assign a weight

$$w_i = \Gamma_i \times p(t_{\text{E},i})p(\theta_{\text{E},i}), \quad (8)$$

where  $\Gamma_i \equiv \theta_{\text{E},i} \mu_{\text{rel},i}$  is the microlensing event rate, and  $p(t_{\text{E},i})$  and  $p(\theta_{\text{E},i})$  are the likelihood factors for  $t_{\text{E},i}$  and  $\theta_{\text{E},i}$  given the probability distributions for each solution.

The physical parameters inferred from the Bayesian analysis are summarized in Table 2 and illustrated in Figure 5. These include the host mass  $M_1$ , the companion (planetary) mass  $M_2$ , the lens distance  $D_L$ , the projected star-planet separation  $a_\perp$ , and the heliocentric lens-source relative proper motion  $\mu_{\text{rel,hel}}$ . The results favor an M-dwarf host located in the Galactic bulge. The companion mass lies between that of Neptune and Saturn, with a projected separation of about 1.6 au. Using a water snow-line scaling of  $a_{\text{SL}} = 2.7(M/M_\odot)$  au (Kennedy & Kenyon 2008), the planet is situated well beyond the snow line.

**Table 2.** Lensing Physical Parameters from a Bayesian Analysis

Model	Physical Properties				
	$M_{\text{host}}(M_{\odot})$	$M_{\text{planet}}(M_{\oplus})$	$D_{\text{L}}(\text{kpc})$	$a_{\perp}(\text{au})$	$\mu_{\text{rel, hel}}(\text{mas yr}^{-1})$
Close Resonant	$0.27^{+0.25}_{-0.14}$	$42.30^{+40.24}_{-22.03}$	$7.5^{+0.7}_{-1.0}$	$1.5^{+0.2}_{-0.2}$	$9.53^{+0.73}_{-0.70}$
Wide Resonant	$0.26^{+0.25}_{-0.14}$	$42.32^{+40.70}_{-22.08}$	$7.5^{+0.7}_{-1.0}$	$1.7^{+0.2}_{-0.2}$	$9.47^{+0.73}_{-0.70}$
Combined	$0.26^{+0.25}_{-0.14}$	$42.32^{+40.62}_{-22.07}$	$7.5^{+0.7}_{-1.0}$	$1.6^{+0.2}_{-0.3}$	$9.48^{+0.73}_{-0.70}$

NOTE—The combined model is obtained by a combination of two models weighted by the probability for the Galactic model and  $\exp(-\Delta\chi^2/2)$ .

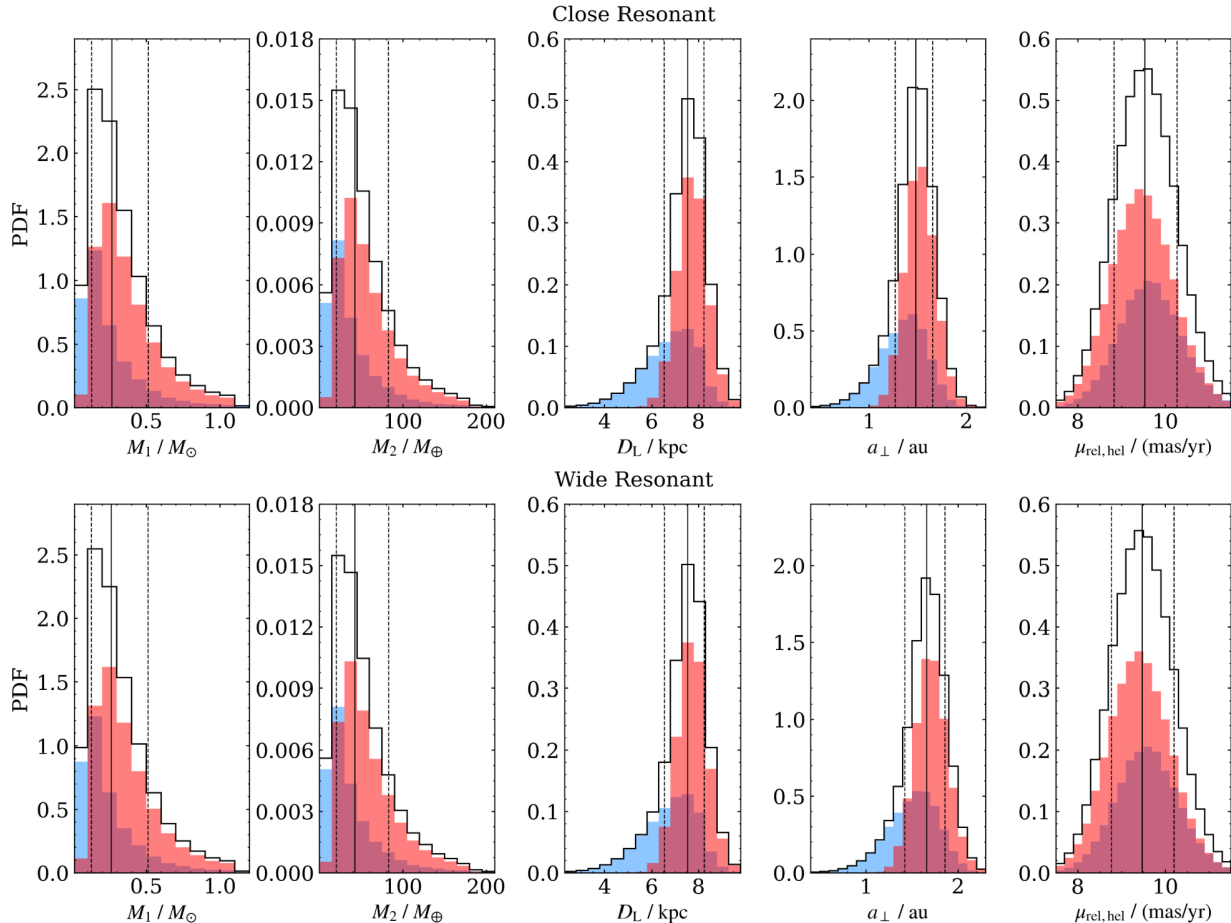


**Figure 5.** Posterior probability distributions from our Bayesian analysis are shown for the host mass  $M_1$ , the planetary mass  $M_2$ , the lens distance  $D_{\text{L}}$ , the projected planet-host separation  $a_{\perp}$ , and the heliocentric lens-source relative proper motion  $\mu_{\text{rel, hel}}$ . In each panel, the solid black curve indicates the median, and the two dashed black curves mark the 15.9% and 84.1% credible limits. Contributions from bulge and disk lens populations are shown in red and blue, respectively.

## 5. DISCUSSION

### 5.1. DREAMS's Role in This Planetary Detection

The anomaly of KMT-2025-BLG-1616 was identified in two independent ways. C. Han detected it using KMTNet's online pySIS photometry, while the DREAMS team independently discovered it by examining the DREAMS light curves of this high-magnification event. We find that the anomaly

from the online photometry can be identified by applying the KMTNet AnomalyFinder algorithm (Zang et al. 2021b, 2022).

We further perform 1L1S and 2L1S modeling without the DREAMS data to check the role of the data (other datasets are identical used in Section 3). Table 3 summarizes the parameters, and Figure 6 shows the corresponding model light curves and residuals. Without the DREAMS data, the

**Table 3.** Lensing Parameters without the DREAMS Data

Parameters	1L1S	2L1S			
		Central		Resonant	
		Close	Wide	Close	Wide
$\chi^2/\text{dof}$	10487.0/10414	<b>10399.5/10411</b>	10399.6/10411	11400.0/10411	11400.0/10411
$t_0 - 10857$ (HJD')	$76423 \pm 0.00033$	<b><math>0.76311 \pm 0.00046</math></b>	$0.76316 \pm 0.00046$	$0.76333 \pm 0.00043$	$0.76329 \pm 0.00044$
$w_0 (10^{-3})$	$7.38 \pm 0.58$	<b><math>7.99 \pm 0.71</math></b>	$7.93 \pm 0.69$	$7.63 \pm 0.71$	$7.61 \pm 0.66$
$t_E$ (days)	$9.46 \pm 0.71$	<b><math>8.08 \pm 0.63</math></b>	$8.12 \pm 0.62$	$8.10 \pm 0.64$	$8.11 \pm 0.60$
$\rho (10^{-3})$	$7.83 \pm 0.63$	<b><math>4.92 \pm 0.42</math></b>	$4.89 \pm 0.42$	$2.36 \pm 0.33$	$2.37 \pm 0.32$
$\alpha$ (rad)	...	<b><math>4.8025 \pm 0.0185</math></b>	$4.8011 \pm 0.0179$	$4.8007 \pm 0.0186$	$4.8003 \pm 0.0184$
$s$	...	<b><math>0.8336 \pm 0.0499</math></b>	$1.2056 \pm 0.0665$	$0.9438 \pm 0.0063$	$1.0684 \pm 0.0076$
$q (10^{-4})$	...	<b><math>4.81 \pm 1.11</math></b>	$4.65 \pm 1.04$	$4.60 \pm 0.82$	$4.64 \pm 0.81$
$\log q$	...	<b><math>-3.318 \pm 0.100</math></b>	$-3.332 \pm 0.097$	$-3.337 \pm 0.077$	$-3.334 \pm 0.076$
$I_S$	$22.282 \pm 0.085$	<b><math>22.011 \pm 0.092</math></b>	$21.991 \pm 0.088$	$22.020 \pm 0.095$	$22.025 \pm 0.090$

light curves also yield two pairs of degenerate 2L1S solutions: “Close Central”, “Wide Central”, “Close Resonant”, and “Wide Resonant”. Their parameters are consistent with those obtained including the DREAMS data (Table 1) within  $1\sigma$ , although the uncertainties in the binary-lens geometry ( $q$ ,  $s$ ,  $\alpha$ ) and  $\rho$  increase by factors of 3–6. Crucially, in the absence of DREAMS data, the “Central/Resonant” degeneracy is severe, with  $\Delta\chi^2 = 0.5$  among the four solutions. Yang et al. (2022) suggested that the  $(\log s, \log q, \alpha)$  phase-space factors can be used to weight the probability of each degenerate solution. For this event, the phase-space factors of the central solutions are approximately 10 times larger than those of the resonant solutions. Therefore, if the DREAMS data were unavailable and the degeneracy were weighted by the phase-space factors, the “Central” solutions would be incorrectly favored.

Therefore, the DREAMS data provide three key contributions to this event. First, they break the “Central/Resonant” degeneracy. Second, they substantially tighten the binary-lens parameters. Third, as shown in Section 4.1, the event is too faint for KMTNet  $V$ -band measurements, and DREAMS’s high-cadence  $r$ -band observations yield a precise source color. The DREAMS  $r - z$  color can be used to constrain source colors in other faint events, even when DREAMS does not cover the planetary anomaly. Moreover, for faint events in high-extinction fields, the combined  $I - z$  color from KMTNet and DREAMS could also constrain the source color.

## 5.2. An Estimate of DREAMS’s Detection Limits for FFPs

The primary motivation of DREAMS is to detect low-mass FFPs with minute-level cadence. Based on the practical photometric accuracy of the DREAMS observations obtained

from this event, we can estimate the minimum FFP masses that DREAMS can detect.

The current plan for DREAMS observations in 2026–2028 will adopt the same survey strategy as the September 2025 run. Specifically, the survey will cover two fields with a  $1 \text{ deg}^2$  overlap. Each field will be observed with four  $z$ -band blocks and one  $r$ -band block per hour, with exposure times of 60 s in  $z$  and 80 s in  $r$ . For estimating the detection limits, we adopt the strategy corresponding to a single field.

The photometric SNRs are taken from the standard deviations of the September 2025 run, with  $\text{SNR} = 26.5$  at  $z_{\text{DECam}} = 18.4$  mag and  $\text{SNR} = 14.7$  at  $r_{\text{DECam}} = 19.4$  mag. For the simulated events we show below, the noise is dominated by sky background from airglow and moonlight, since DREAMS operates during DECam bright time. Consequently, despite variations in extinction and stellar surface density across the DREAMS fields, these photometric error bars remain applicable. The SNRs for different brightness are estimated by

$$\text{SNR}(z_{\text{DECam}}) = 26.5 \times 10^{(18.4 - z_{\text{DECam}})/2.5}, \quad (9)$$

$$\text{SNR}(r_{\text{DECam}}) = 14.7 \times 10^{(19.4 - r_{\text{DECam}})/2.5}. \quad (10)$$

The DREAMS survey fields are located at  $-1.0 \lesssim \ell \lesssim 2.0$  and  $-2.8 \lesssim b \lesssim -0.6$ , with a central position at approximately  $(\ell, b) = (0.5, -1.8)$ . We adopt a representative extinction of  $A_I = 1.8$  and a reddening of  $E(V - I) = 1.55$ , which are close to the extinction values at the field center (Nataf et al. 2013) and are lower than those of the field surrounding KMT-2025-BLG-1616. To transform DECam instrumental magnitudes to the standard  $V$  and  $I$  system commonly used, we match bright field stars in common between

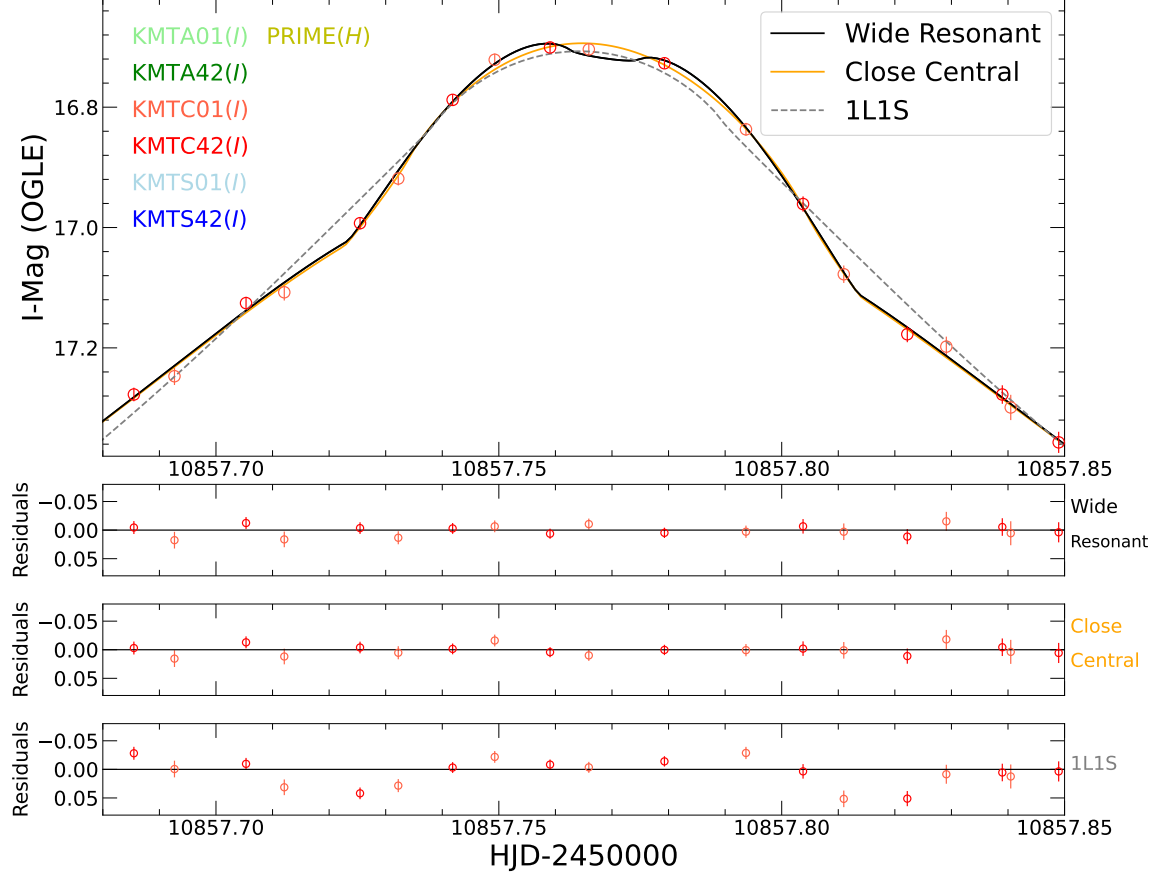


**Figure 6.** A close-up of the anomaly and models excluding the DREAMS data. The symbols are similar to those in Figure 1. The parameters are shown in Table 3.

DREAMS and OGLE-III and obtain

$$z_{\text{DECam}} = I - 0.55 - 0.24(V - I), \quad (11)$$

$$r_{\text{DECam}} = I - 1.75 + 0.53(V - I). \quad (12)$$

We first consider DREAMS's sensitivity to Mars-mass FFPs in the Galactic bulge. We adopt a typical bulge configuration with  $D_S = 8.5$  kpc,  $D_L = 7.0$  kpc, and  $\mu_{\text{rel}} = 6.5$  mas yr $^{-1}$  (The proper motion value is adopted from Gould et al. 2021). We simulate three cases with source brightnesses  $I = 18.0, 19.5$ , and  $20.5$ , respectively; their colors are assigned as the median color of *HST* field stars whose extinction-corrected magnitudes are within 0.1 mag of the corresponding source.

Figure 7 displays the simulated light curves. We bin the data within each cadence group into a single point. All cases satisfy the FFP detection criteria adopted in the *Roman* FFP simulations (Johnson et al. 2020): (1) at least six data points exceed the baseline flux by  $\geq 3\sigma$ ; and (2) the  $\chi^2$  difference between a flat model and the best-fit 1L1S model is  $\geq 300$ . The  $I = 20.5$  case yields the smallest  $\Delta\chi^2$  and lies closest to the detection threshold, implying that, for a typical DREAMS field, sources with  $I \lesssim 20.5$  are sensitive to Mars-

mass FFPs. For the  $I = 18$  source, the  $z$ -band points rise to  $\sim 4\sigma$  above baseline for a Mars-mass FFP. Scaling to a  $3\sigma$  criterion therefore reduces the corresponding mass to  $3/4 M_{\text{Mars}}$ , and the resulting  $\Delta\chi^2 \sim 390$  remains above the detection limit. A comparable threshold mass is obtained for the  $I = 19.5$  source, for which the  $\Delta\chi^2$  requirement sets the detection limit.

Because disk lenses have larger  $\theta_E$ , Mars-mass FFPs in the disk yield higher SNRs. We therefore investigate whether Moon-mass FFPs can be detected by DREAMS. The lower right panel of Figure 7 shows a simulated light curve for a Moon-mass FFP with an  $I = 19.5$  source and  $D_L = 3.2$  kpc. We adopt a slightly larger lens-source relative proper motion,  $\mu_{\text{rel}} = 8$  mas yr $^{-1}$ . The simulated light curve contains 10 data points that exceed the baseline flux by  $\geq 3\sigma$  and yields  $\Delta\chi^2 = 370$ , indicating that DREAMS is sensitive to disk Moon-mass FFPs. In the 1 deg $^2$  region where the two DREAMS fields overlap, the cadence is double and thus DREAMS is sensitive to planets less massive than the Moon. Lower extinction increases the source flux received by DECam and thus enables sensitivity to less-massive FFPs; conversely, higher extinction reduces the sensitivity. We have been developing the DREAMS full-frame imaging pipeline

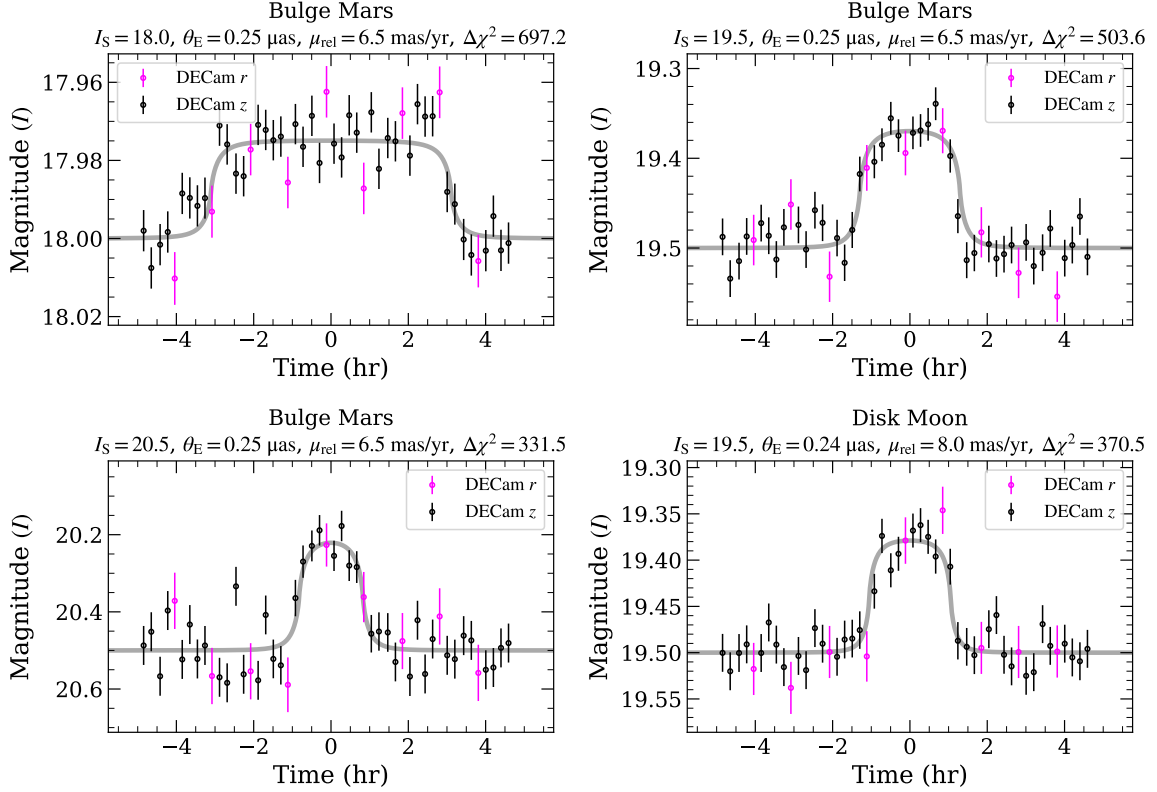


**Figure 7.** Simulated FFP events as observed by DREAMS. For clarity, data within each observing block are binned (four points in \$z\$ and three in \$r\$ per block). Magnitudes are placed on the \$I\$-band scale. Lens and source for each panel parameters are summarized in Table 4. \$\Delta\chi^2\$ denotes the difference in \$\chi^2\$ between a flat model and the best-fit 1L1S model.

following the framework of Qian et al. (2025), and we expect to complete the FFP search for 2025 observations by early 2026.

H.Y. acknowledge support by the China Postdoctoral Science Foundation (No. 2024M762938). W.Z. acknowledges the support from the Harvard-Smithsonian Center for Astrophysics through the CfA Fellowship. H.Y., W.Z., J.Z., H.L., Y.T., Q.Q., Z.L., Y.S., X.S. and S.M. acknowledge support by the National Natural Science Foundation of China (Grant No. 12133005). This work is part of the ET space mission which is funded by the China’s Space Origins Exploration Program. This research has made use of the KMTNet system operated by the Korea Astronomy and Space Science Institute (KASI) at three host sites of CTIO in Chile, SAAO in South Africa, and SSO in Australia. Data transfer from the host site to KASI was supported by the Korea Research Environment Open NETwork (KREONET). This research was supported by KASI under the R&D program (project No. 2025-1-830-05) supervised by the Ministry of Science and ICT. The PRIME project is supported by JSPS KAKENHI Grant Number JP16H06287, JP22H00153, JP25H00668, JP19KK0082, JP20H04754, JP24H01811 and JPJSCCA20210003. The PRIME project acknowledges a financial support by Astrobiology Center. Work by J.C.Y. acknowledge support from N.S.F Grant No. AST-2108414. Work by C.H. was supported by the grants of National Research Foundation of Korea (2019R1A2C2085965 and 2020R1A4A2002885). Y.S.

**Table 4.** Lens and Source Information for Simulated Events

Parameters	Bulge Mars			Disk Moon
\$I_S\$	18.00	19.50	20.50	19.50
\$V_S\$	20.50	21.80	22.80	21.80
\$z_{\text{DECam}}\$	16.85	18.40	19.40	18.40
\$r_{\text{DECam}}\$	17.55	18.95	19.95	18.95
\$D_S\$ (kpc)	8.5	8.5	8.5	8.5
\$\theta_*\$ (\$\mu\text{as}\$)	2.3	0.96	0.61	0.96
\$M_L (M_\oplus)\$	0.107	0.107	0.107	0.0123
\$D_L\$ (kpc)	7.0	7.0	7.0	3.2
\$\theta_E\$ (\$\mu\text{as}\$)	0.25	0.25	0.25	0.24
\$\mu_{\text{rel}} (\text{mas yr}^{-1})\$	6.5	6.5	6.5	8.0

NOTE—Assume \$A\_I = 1.8\$ and \$E(V - I) = 1.55\$.

acknowledges support from BSF Grant No. 2020740. RAS and KK acknowledge support from US National Science Foundation grant 2206828.

This project used data obtained with the Dark Energy Camera (DECam), which was constructed by the Dark Energy Survey (DES) collaboration. Funding for the DES Projects has been provided by the U.S. Department of Energy, the U.S. National Science Foundation, the Ministry of Science and Education of Spain, the Science and Technology Facilities Council of the United Kingdom, the Higher Education Funding Council for England, the National Center for Supercomputing Applications at the University of Illinois at Urbana-Champaign, the Kavli Institute for Cosmological Physics at the University of Chicago, the Center for Cosmology and Astro-Particle Physics at The Ohio State University, the Mitchell Institute for Fundamental Physics and Astronomy at Texas A&M University, Financiadora de Estudos e Projetos, Fundação Carlos Chagas Filho de Amparo à Pesquisa do Estado do Rio de Janeiro, Conselho Nacional de Desenvolvimento Científico e Tecnológico and the Ministério da Ciência, Tecnologia e Inovação, the Deutsche Forschungsgemeinschaft, and the collaborating institutions in the Dark Energy Survey.

The collaborating institutions are Argonne National Laboratory; the University of California at Santa Cruz; the University of Cambridge; Centro de Investigaciones Energéticas, Medioambientales y Tecnológicas (CIEMAT), Madrid; the University of Chicago; University College Lon-

don; the DES-Brazil Consortium; the University of Edinburgh; the Eidgenössische Technische Hochschule (ETH) Zürich; Fermi National Accelerator Laboratory; the University of Illinois at Urbana-Champaign; the Institut de Ciències de l'Espai (IEEC/CSIC); the Institut de Física d'Altes Energies (IFAE); Lawrence Berkeley National Laboratory; the Ludwig-Maximilians-Universität München and the associated Excellence Cluster Universe; the University of Michigan; NSF NOIRLab; the University of Nottingham; The Ohio State University; the OzDES Membership Consortium; the University of Pennsylvania; the University of Portsmouth; SLAC National Accelerator Laboratory; Stanford University; the University of Sussex; and Texas A&M University.

Based on observations at NSF Cerro Tololo Inter-American Observatory, NSF NOIRLab (NOIRLab Prop. ID 2025A-806294, PI: Weicheng Zang; Prop. ID 2025B-560332, PI: Weicheng Zang & Hongjing Yang), which is managed by the Association of Universities for Research in Astronomy (AURA) under a cooperative agreement with the U.S. National Science Foundation.

*Software:* pySIS (Albrow et al. 2009; Yang et al. 2024, 2025), numpy (Harris et al. 2020), emcee (Goodman & Weare 2010; Foreman-Mackey et al. 2013), Matplotlib (Hunter 2007), SciPy (Virtanen et al. 2020), galpy (Bovy 2015), DECam Community Pipeline (Valdes et al. 2014)

## REFERENCES

Adams, A. D., Boyajian, T. S., & von Braun, K. 2018, MNRAS, 473, 3608, doi: [10.1093/mnras/stx2367](https://doi.org/10.1093/mnras/stx2367)

Alard, C., & Lupton, R. H. 1998, ApJ, 503, 325, doi: [10.1086/305984](https://doi.org/10.1086/305984)

Albrow, M. D., Horne, K., Bramich, D. M., et al. 2009, MNRAS, 397, 2099, doi: [10.1111/j.1365-2966.2009.15098.x](https://doi.org/10.1111/j.1365-2966.2009.15098.x)

An, J. H., Albrow, M. D., Beaulieu, J.-P., et al. 2002, ApJ, 572, 521, doi: [10.1086/340191](https://doi.org/10.1086/340191)

Beaulieu, J.-P., Bennett, D. P., Fouqué, P., et al. 2006, Nature, 439, 437, doi: [10.1038/nature04441](https://doi.org/10.1038/nature04441)

Bell, A., Zhang, J., Zang, W., et al. 2024, PASP, 136, 054402, doi: [10.1088/1538-3873/ad48b8](https://doi.org/10.1088/1538-3873/ad48b8)

Bennett, D. P., Bond, I. A., Udalski, A., et al. 2008, ApJ, 684, 663, doi: [10.1086/589940](https://doi.org/10.1086/589940)

Bensby, T., Yee, J. C., Feltzing, S., et al. 2013, A&A, 549, A147, doi: [10.1051/0004-6361/201220678](https://doi.org/10.1051/0004-6361/201220678)

Bond, I. A., Abe, F., Dodd, R. J., et al. 2001, MNRAS, 327, 868, doi: [10.1046/j.1365-8711.2001.04776.x](https://doi.org/10.1046/j.1365-8711.2001.04776.x)

Bovy, J. 2015, ApJS, 216, 29, doi: [10.1088/0067-0049/216/2/29](https://doi.org/10.1088/0067-0049/216/2/29)

Bozza, V. 2010, MNRAS, 408, 2188, doi: [10.1111/j.1365-2966.2010.17265.x](https://doi.org/10.1111/j.1365-2966.2010.17265.x)

Bozza, V., Bachelet, E., Bartolić, F., et al. 2018, MNRAS, 479, 5157, doi: [10.1093/mnras/sty1791](https://doi.org/10.1093/mnras/sty1791)

Bozza, V., Saggese, V., Covone, G., Rota, P., & Zhang, J. 2025, A&A, 694, A219, doi: [10.1051/0004-6361/202452648](https://doi.org/10.1051/0004-6361/202452648)

Cassan, A., Kubas, D., Beaulieu, J. P., et al. 2012, Nature, 481, 167, doi: [10.1038/nature10684](https://doi.org/10.1038/nature10684)

Christiansen, J. L., McElroy, D. L., Harbut, M., et al. 2025, arXiv e-prints, arXiv:2506.03299. <https://arxiv.org/abs/2506.03299>

Claret, A., & Bloemen, S. 2011, A&A, 529, A75, doi: [10.1051/0004-6361/201116451](https://doi.org/10.1051/0004-6361/201116451)

Dong, S., Gould, A., Udalski, A., et al. 2009, ApJ, 695, 970, doi: [10.1088/0004-637X/695/2/970](https://doi.org/10.1088/0004-637X/695/2/970)

Flaughler, B., Diehl, H. T., Honscheid, K., et al. 2015, AJ, 150, 150, doi: [10.1088/0004-6256/150/5/150](https://doi.org/10.1088/0004-6256/150/5/150)

Foreman-Mackey, D., Hogg, D. W., Lang, D., & Goodman, J. 2013, PASP, 125, 306, doi: [10.1086/670067](https://doi.org/10.1086/670067)

Goodman, J., & Weare, J. 2010, Communications in Applied Mathematics and Computational Science, 5, 65, doi: [10.2140/camcos.2010.5.65](https://doi.org/10.2140/camcos.2010.5.65)

Gould, A. 1992, ApJ, 392, 442, doi: [10.1086/171443](https://doi.org/10.1086/171443)

—. 1994, ApJL, 421, L75, doi: [10.1086/187191](https://doi.org/10.1086/187191)

—. 2000, ApJ, 542, 785, doi: [10.1086/317037](https://doi.org/10.1086/317037)

Gould, A., & Loeb, A. 1992, ApJ, 396, 104, doi: [10.1086/171700](https://doi.org/10.1086/171700)

Gould, A., Zang, W.-C., Mao, S., & Dong, S.-B. 2021, Research in Astronomy and Astrophysics, 21, 133, doi: [10.1088/1674-4527/21/6/133](https://doi.org/10.1088/1674-4527/21/6/133)

Gould, A., Dong, S., Gaudi, B. S., et al. 2010, ApJ, 720, 1073, doi: [10.1088/0004-637X/720/2/1073](https://doi.org/10.1088/0004-637X/720/2/1073)

Gould, A., Jung, Y. K., Hwang, K.-H., et al. 2022, Journal of Korean Astronomical Society, 55, 173, doi: [10.5303/JKAS.2022.55.5.173](https://doi.org/10.5303/JKAS.2022.55.5.173)

Griest, K., & Safizadeh, N. 1998, ApJ, 500, 37, doi: [10.1086/305729](https://doi.org/10.1086/305729)

Harris, C. R., Millman, K. J., van der Walt, S. J., et al. 2020, Nature, 585, 357, doi: [10.1038/s41586-020-2649-2](https://doi.org/10.1038/s41586-020-2649-2)

Holtzman, J. A., Watson, A. M., Baum, W. A., et al. 1998, AJ, 115, 1946, doi: [10.1086/300336](https://doi.org/10.1086/300336)

Honscheid, K., & DePoy, D. L. 2008, arXiv e-prints, arXiv:0810.3600, doi: [10.48550/arXiv.0810.3600](https://doi.org/10.48550/arXiv.0810.3600)

Houdashelt, M. L., Bell, R. A., & Sweigart, A. V. 2000, AJ, 119, 1448, doi: [10.1086/301243](https://doi.org/10.1086/301243)

Hunter, J. D. 2007, Computing in Science & Engineering, 9, 90, doi: [10.1109/MCSE.2007.55](https://doi.org/10.1109/MCSE.2007.55)

Johnson, S. A., Penny, M., Gaudi, B. S., et al. 2020, AJ, 160, 123, doi: [10.3847/1538-3881/aba75b](https://doi.org/10.3847/1538-3881/aba75b)

Kennedy, G. M., & Kenyon, S. J. 2008, ApJ, 673, 502, doi: [10.1086/524130](https://doi.org/10.1086/524130)

Kim, D.-J., Kim, H.-W., Hwang, K.-H., et al. 2018a, AJ, 155, 76, doi: [10.3847/1538-3881/aaa47b](https://doi.org/10.3847/1538-3881/aaa47b)

Kim, H.-W., Hwang, K.-H., Shvartzvald, Y., et al. 2018b, arXiv e-prints, arXiv:1806.07545. <https://arxiv.org/abs/1806.07545>

Kim, S.-L., Lee, C.-U., Park, B.-G., et al. 2016, Journal of Korean Astronomical Society, 49, 37, doi: [10.5303/JKAS.2016.49.1.037](https://doi.org/10.5303/JKAS.2016.49.1.037)

Koshimoto, N., Sumi, T., Bennett, D. P., et al. 2023, AJ, 166, 107, doi: [10.3847/1538-3881/ace689](https://doi.org/10.3847/1538-3881/ace689)

Kroupa, P. 2001, MNRAS, 322, 231, doi: [10.1046/j.1365-8711.2001.04022.x](https://doi.org/10.1046/j.1365-8711.2001.04022.x)

Mao, S., & Paczynski, B. 1991, ApJL, 374, L37, doi: [10.1086/186066](https://doi.org/10.1086/186066)

Mróz, P., A., Skowron, J., et al. 2017, Nature, 548, 183, doi: [10.1038/nature23276](https://doi.org/10.1038/nature23276)

Mróz, P., Poleski, R., Gould, A., et al. 2020, ApJL, 903, L11, doi: [10.3847/2041-8213/abbfad](https://doi.org/10.3847/2041-8213/abbfad)

Nataf, D. M., Gould, A., Fouqué, P., et al. 2013, ApJ, 769, 88, doi: [10.1088/0004-637X/769/2/88](https://doi.org/10.1088/0004-637X/769/2/88)

Nemiroff, R. J., & Wickramasinghe, W. A. D. T. 1994, ApJL, 424, L21, doi: [10.1086/187265](https://doi.org/10.1086/187265)

Paczyński, B. 1986, ApJ, 304, 1, doi: [10.1086/164140](https://doi.org/10.1086/164140)

Poleski, R., Skowron, J., Mróz, P., et al. 2021, AcA, 71, 1, doi: [10.32023/0001-5237/71.1.1](https://doi.org/10.32023/0001-5237/71.1.1)

Qian, Q., Yang, H., Zang, W., et al. 2025, PASP, 137, 064401, doi: [10.1088/1538-3873/add9cf](https://doi.org/10.1088/1538-3873/add9cf)

Sako, T., Sekiguchi, T., Sasaki, M., et al. 2008, Experimental Astronomy, 22, 51, doi: [10.1007/s10686-007-9082-5](https://doi.org/10.1007/s10686-007-9082-5)

Shvartzvald, Y., Maoz, D., Udalski, A., et al. 2016, MNRAS, 457, 4089, doi: [10.1093/mnras/stw191](https://doi.org/10.1093/mnras/stw191)

Sumi, T., Kamiya, K., Bennett, D. P., et al. 2011, Nature, 473, 349, doi: [10.1038/nature10092](https://doi.org/10.1038/nature10092)

Sumi, T., Koshimoto, N., Bennett, D. P., et al. 2023, AJ, 166, 108, doi: [10.3847/1538-3881/ace688](https://doi.org/10.3847/1538-3881/ace688)

Sumi, T., Buckley, D. A. H., Kutyrev, A. S., et al. 2025, arXiv e-prints, arXiv:2508.14474, doi: [10.48550/arXiv.2508.14474](https://doi.org/10.48550/arXiv.2508.14474)

Suzuki, D., Bennett, D. P., Sumi, T., et al. 2016, ApJ, 833, 145, doi: [10.3847/1538-4357/833/2/145](https://doi.org/10.3847/1538-4357/833/2/145)

Szymański, M. K., Udalski, A., Soszyński, I., et al. 2011, AcA, 61, 83. <https://arxiv.org/abs/1107.4008>

Tomaney, A. B., & Crots, A. P. S. 1996, AJ, 112, 2872, doi: [10.1086/118228](https://doi.org/10.1086/118228)

Udalski, A., Szymański, M. K., & Szymański, G. 2015, AcA, 65, 1. <https://arxiv.org/abs/1504.05966>

Udalski, A., Jaroszyński, M., Paczyński, B., et al. 2005, ApJL, 628, L109, doi: [10.1086/432795](https://doi.org/10.1086/432795)

Valdes, F., Gruendl, R., & DES Project. 2014, in Astronomical Society of the Pacific Conference Series, Vol. 485, Astronomical Data Analysis Software and Systems XXIII, ed. N. Manset & P. Forshay, 379

Virtanen, P., Gommers, R., Oliphant, T. E., et al. 2020, Nature Methods, 17, 261, doi: [10.1038/s41592-019-0686-2](https://doi.org/10.1038/s41592-019-0686-2)

Witt, H. J., & Mao, S. 1994, ApJ, 430, 505, doi: [10.1086/174426](https://doi.org/10.1086/174426)

Yang, H., Mao, S., Zang, W., & Zhang, X. 2021, MNRAS, 502, 5631, doi: [10.1093/mnras/stab441](https://doi.org/10.1093/mnras/stab441)

Yang, H., Zang, W., Gould, A., et al. 2022, MNRAS, 516, 1894, doi: [10.1093/mnras/stac2023](https://doi.org/10.1093/mnras/stac2023)

Yang, H., Yee, J. C., Hwang, K.-H., et al. 2024, MNRAS, 528, 11, doi: [10.1093/mnras/stad3672](https://doi.org/10.1093/mnras/stad3672)

Yang, H., Yee, J. C., Zhang, J., et al. 2025, AJ, 169, 295, doi: [10.3847/1538-3881/adc73e](https://doi.org/10.3847/1538-3881/adc73e)

Yee, J. C., Shvartzvald, Y., Gal-Yam, A., et al. 2012, ApJ, 755, 102, doi: [10.1088/0004-637X/755/2/102](https://doi.org/10.1088/0004-637X/755/2/102)

Yee, J. C., Zang, W., Udalski, A., et al. 2021, AJ, 162, 180, doi: [10.3847/1538-3881/ac1582](https://doi.org/10.3847/1538-3881/ac1582)

Yoo, J., DePoy, D. L., Gal-Yam, A., et al. 2004, ApJ, 603, 139, doi: [10.1086/381241](https://doi.org/10.1086/381241)

Zang, W., Han, C., Kondo, I., et al. 2021a, Research in Astronomy and Astrophysics, 21, 239, doi: [10.1088/1674-4527/21/9/239](https://doi.org/10.1088/1674-4527/21/9/239)

Zang, W., Hwang, K.-H., Udalski, A., et al. 2021b, AJ, 162, 163,  
doi: [10.3847/1538-3881/ac12d4](https://doi.org/10.3847/1538-3881/ac12d4)

Zang, W., Yang, H., Han, C., et al. 2022, MNRAS, 515, 928,  
doi: [10.1093/mnras/stac1883](https://doi.org/10.1093/mnras/stac1883)

Zang, W., Jung, Y. K., Yee, J. C., et al. 2025, Science, 388, 400,  
doi: [10.1126/science.adn6088](https://doi.org/10.1126/science.adn6088)

Zhang, J., Zang, W., Jung, Y. K., et al. 2023, MNRAS, 522, 6055,  
doi: [10.1093/mnras/stad1398](https://doi.org/10.1093/mnras/stad1398)

Zhu, W., Udalski, A., Calchi Novati, S., et al. 2017, AJ, 154, 210,  
doi: [10.3847/1538-3881/aa8ef1](https://doi.org/10.3847/1538-3881/aa8ef1)